High-resolution Ambient Noise Tomography of Shallow Fault Zones Along the July 2019 Ridgecrest Ruptures

Zheng Zhou[1]; Michael Bianco[1]; Peter Gerstoft[1]; Kim Olsen[2]

[1]University of California, San Diego; [2]San Diego State University

Abstract

We perform ambient noise tomography (ANT) using data recorded on 342 seismographs within a 50x50 km area inside which the July 2019 M7.1 and M6.4 Ridgecrest earthquakes occurred. We used the locally sparse tomography (LST) method, an unsupervised machine learning approach that learns to represent small scale geophysical structures directly from measurements. The Rayleigh group speed obtained from LST better predicts travel times than conventional regularized least-squares inversion. The 3D shear velocity model of the area obtained from the surface wave dispersion maps reveals a highly heterogeneous, up to 5 km wide and at least 5 km deep low velocity zone around the causative faults for the M7.1 and M6.4 events, with a 40% reduction of Rayleigh wave velocity. The extent of the LVZ is consistent with the observed complex and distributed active faulting observed along the 2019 Ridgecrest ruptures and ambient noise imaging in other regions.

Data and Preprocessing

- We use seismic signals recorded from 07/13/2019 to 09/08/2019 around the Ridgecrest area.
- 342 nodes in total: 65 sparse arrays with ~8-15 km intervals and 277 dense arrays with ~60-170 m intervals.
- The raw seismic signals are filtered by 1 Hz low-pass filter to reduce the high frequency noise.
- Noise cross-correlation is performed to extract the travel time information.

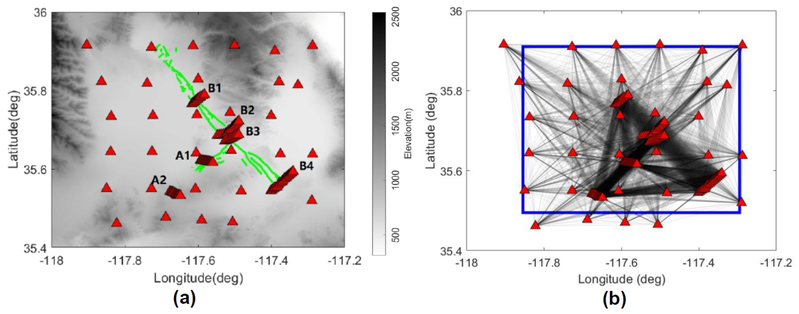

Figure 1. (a) The red triangles represent the locations of the Nodal arrays in the Ridgecrest area used in our study, and the green lines denote the fault traces from field mapping [2]. (b) The ray coverage in the model region (blue box).

Gobal Slowness and Travel Time

The slowness pixels are represented by the vector $s' = s_0 + s_g \in R^N$, where s_0 is the reference slowness and s_g is the perturbation from the reference. The travel time observations can be expressed as $t' = t_0 + t_g \in R^M$, where t_0 and t_g are the reference travel times and perturbations.

Since s_0 and $t_0 = As_0$ are known (where $A \in R^{M \times N}$ is the tomography matrix), we estimate the perturbations

$$t = As_g + \varepsilon, \qquad (1)$$

where $\varepsilon \in R^M$ is 0-mean Gaussian noise.

Locally-sparse Model

Different from the conventional gobal tomography, we introduce an additional slowness vector $s_s \in R^N$ to capture the local slowness features[1]. Here $D \in R^{n \times Q}$ is a dictionary of Q atoms, and $x_i \in R^n$ are the sparse coefficients with n the number of pixels in a patch. $R_i \in \{0,1\}^{n \times N}$ is a binary matrix which selects a particular patch from s_s .

$$\{\hat{s}_g, \hat{s}_s, \hat{\mathbf{X}}\} = \arg\min_{s_g, s_s, X} \left\{ \frac{1}{\sigma_\varepsilon^2} \left\| \mathbf{w}(t - \mathbf{A}s_g) \right\|_2^2 + \frac{1}{\sigma_s^2} \left\| s_s - s_g \right\|_2^2 + \frac{1}{\sigma_p^2} \sum_i \left\| \mathbf{D}x_i - \mathbf{R}_i s_s \right\|_2^2 \right\}, \quad (2)$$

subject to $\|x_i\|_0 = T, \forall i.$

with $\hat{\mathbf{X}} = [\hat{x}_1, \hat{x}_2, \ldots, \hat{x}_I]$ and $\sigma_\varepsilon, \sigma_s, \sigma_p$ being parameters related to variance. **w** is the ray-azimuth-distribution normalization vector.

Results

We derive a velocity map via taking the reciprocal of the slowness map generated by our LST method, and use a least-square method (LSQ, in Fig.4) and surface wave dispersion inversion (in Fig.5) as the baseline. All the results are derived under a 10-fold cross validation policy. The width of the LVZs vary from 1 to 5 km.

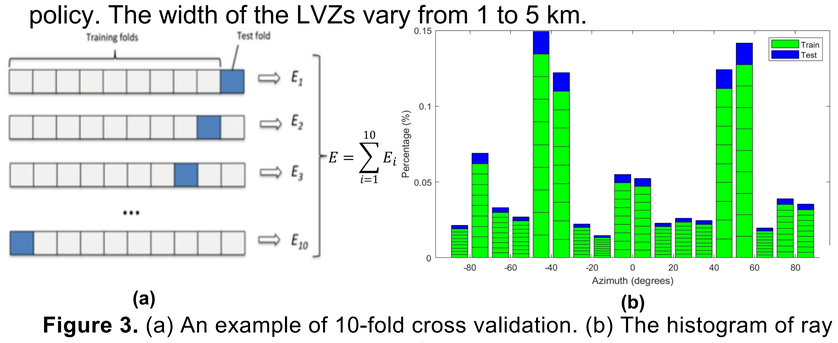

Figure 3. (a) An example of 10-fold cross validation. (b) The histogram of ray azimuths for distributions, and each fold data are proportional to the azimuth distribution.

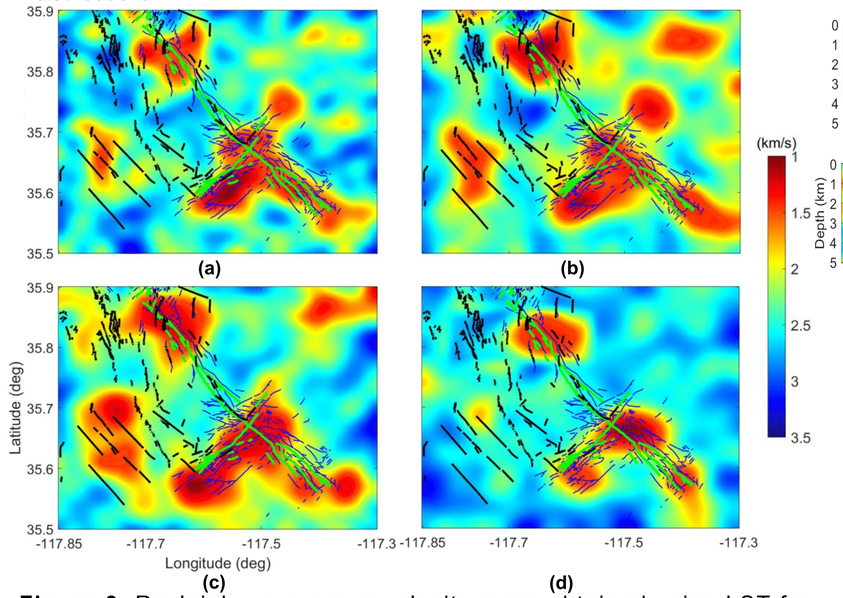

Figure 3. Rayleigh wave group velocity maps obtained using LST for bandwidths (a) 0.02-1 Hz, (b) 0.7-0.9 Hz, (c) 0.5-0.7 Hz, and (d) 0.2-0.5 Hz, with the M7.1 and 6.4 fault traces (green lines) [2], phase gradients (blue traces) [3], and additional Quaternary fault traces (black lines) [4] superimposed.

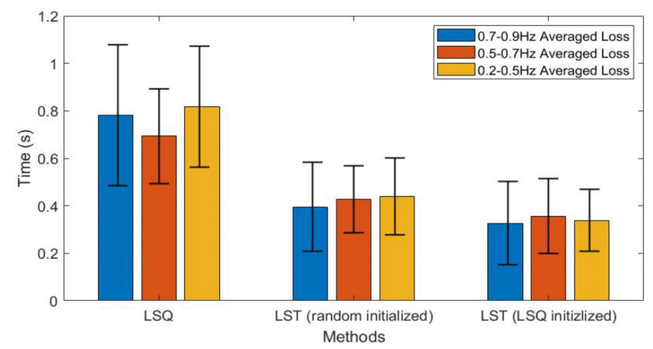

Figure 4. (a) The Rayleigh wave group velocity maps for 0.7-0.9 Hz, 0.5-0.7 Hz, and 0.2-0.5 Hz with the 2 km/s contour lines (white) superimposed. The difference maps are superimposed with the main fault traces (in green), phase gradients (in blue), and the 2 km/s contour lines from the LST maps. (b) 10 fold-averaged mean (bins) and standard deviation (errorbars) of the normalized travel time residual losses derived by the LSQ and LST.

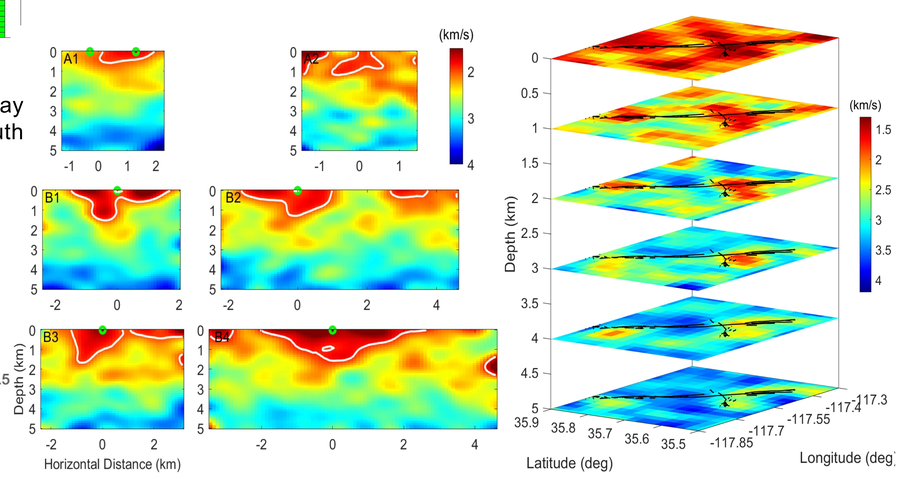

Figure 5. (a) Vertical cross section of the shear wave velocities from the A1, A2, B1, B2, B3 and B4 station arrays. The intersection with the surface rupture of the M6.4 and M7.1 Ridgecrest events (green circles) and 2 km/s contours (white lines) are indicated. (b) Composite 3D image of shear wave velocities obtained from inversion of Rayleigh waves dispersion curves, delineating flower-shaped LVZs.

Summary

Our Rayleigh phase velocity map of the upper 5 km in the Ridgecrest area using ambient noise reveals 1-5 km wide low-velocity zones (LVZs) surrounding parts of the 2019 M7.1 and M6.4 earthquakes. These LVZs correlate well with the distributed area of surface traces mapped from phase gradients of the Sentinel1 radar satellite. Our results suggest a highly heterogeneous fault damage zone for the 2019 sequence. In addition, correlation of other imaged LVZs with parts of the Little Lake Fault system without recent activity suggest long-lasting damage zones.

References

[1]. Bianco, M.J. and Gerstoft, P., 2018. Travel time tomography with adaptive dictionaries. IEEE Transactions on Computational Imaging, 4(4), pp.499-511.

[2] Milliner, C. and Donnellan, A., 2020. Using Daily Observations from Planet Labs Satellite Imagery to Separate the Surface Deformation between the 4 July M w 6.4 Foreshock and 5 July M w 7.1 Mainshock during the 2019 Ridgecrest Earthquake Sequence. Seismological Research Letters.

[3]. Allam, A.A., R.D. Catchings, J.H. Steidl, E.M. Berg, N. Downey, Y. Ben-Zion, M.R. Goldman, J.H. Chan, C.J. Criley, D. Langermann, A.T. McEvilly, Z. Ma, D.D. Mongovin, A Multiscale Seismic Deployment with 463 Sensors Following the 2019 Ridgecrest Earthquake Sequence in Eastern CA , 2019 SCEC poster.

[4] Kohler, M. D. (2003). Mantle Heterogeneities and the SCEC Reference Three-Dimensional Seismic Velocity Model Version, Bulletin of the Seismological Society of America 93.2, 757–774.

[5]. Zhou, Z., and Bianco, M. J., and Gerstoft, P., and Olsen, K. B., 2021. High-resolution Imaging of Complex Shallow Fault Zones Along the July 2019 Ridgecrest Ruptures. Geophysical Research Letters (under review).

Acknowledgements

The research is supported by SCEC award 20140.